Journal of Asian Earth Sciences 86 (2014) 12–24

Contents lists available at ScienceDirect

Journal of Asian Earth Sciences

journal homepage: www.elsevier.com/locate/jseaes

Fluid overpressure along an Oligocene out-of-sequence thrust in the Shimanto Belt, SW Japan

François X. Passelègue [a,b,*], Olivier Fabbri [a], Michel Dubois [c], Sandra Ventalon [d]

[a] UMR CNRS 6249, Université de Franche-Comté, 16 route de Gray, 25030 Besançon, France
[b] UMR8538, Laboratoire de Géologie de l'École Normale Supérieure, 75005 Paris, France
[c] Laboratoire de Génie Civil et géo-Environnement (LGCgE/EA4515), building SN5, University Lille 1, 59655 Villeneuve d'Ascq, France
[d] UFR Sciences de la Terre, Cité Scientifique, 59655 Villeneuve d'Ascq, France

ARTICLE INFO

Article history:
Available online 28 October 2013

Keywords:
Accretionay prism
Out-of-sequence thrust fault
Fault breccia
Fluid
Hydraulic fracturing
Japan
Oligocene

ABSTRACT

Out-of-sequence thrusts (OSTs) exposed in ancient accretionary prisms are considered as fossil analogs of present-day megasplay faults in subduction margins and can provide direct information about the conditions of deformation during thrust activity. In modern as well as in ancient accretionary prisms, first-order megasplay faults or OSTs truncate or merge with faults of lesser importance called second-order OSTs. Structural analysis of the Makinokuchi fault, a branch of an Oligocene to lower Miocene second-order OST in the Tertiary Shimanto Belt of central Kyushu, SW Japan, brings information about the conditions of deformation at the time of thrusting. The studied exposure shows that the fault footwall and, to a much lesser extent, the fault hanging-wall, consist of quartz-cemented syntectonic dilatant hydraulic breccias testifying to pore fluid pressures larger than the least principal stress component. The footwall sandstones are crossed by several centimeters thick quartz veins that merge with the footwall breccias. The continuity between the veins and the breccias suggest that the veins acted as conduits which likely collected fluids from the footwall side sandstones upward and toward the fault. Fluid inclusions indicate that the quartz cementing the breccias and that filling the feeder veins crystallized from similar fluids and under similar pressure and temperature conditions (245–285 °C and 5–8 km depth). These similarities suggest that the fluids responsible for syn-tectonic hydraulic brecciation were collected from the footwall through the conduits. The fluid inclusion trapping temperatures are close to the temperatures expected to be reached along the seismogenic zone. Our analysis shows that fluid overpressures can play a key role in the growth and activity of second-order OSTs in accretionary prisms and suggests that fluids collected along second-order OSTs or splay faults may flow upward along first-order OSTs or megasplay faults.

1. Introduction

Megasplay faults crossing accretionary prisms (Moore et al., 1991; Park et al., 2000, 2002; Collot et al., 2008; Hsu et al., 2013) are suspected to propagate seismic ruptures from the plate interface upward and could therefore be responsible for strong motions in coastal areas and for the triggering of major tsunamis. Recent examples of such possible trajectories include the 1944 Tonankai earthquake (Tanioka and Satake, 2001), the 1946 Nankaido earthquake (Cummins and Kaneda, 2000; Cummins et al., 2001; Park et al., 2000, 2002), the 1964 Alaska earthquake (Plafker, 1972), the 2004 Sumatra earthquake (Waldhauser et al., 2012) or the 2010 Maule earthquake (Melnick et al., 2012).

In addition to their possible role in conveying large interplate ruptures upwards, megasplay faults seem to be the site of very low frequency (VLF) earthquakes and, as such, may mechanically interact with the deep parts of the plate interfaces by releasing a part of the strain. This has been recognized in the Nankai accretionary prism (Ito and Obara, 2006a; Obana and Kodaira, 2009). The Nankai VLF earthquakes nucleating in the vicinity of the emerging megasplay fault recognized there are characterized by very low stress drops, suggesting a weakening of the faults by fluids (Ito and Obara, 2006b).

The shallow parts of megasplay faults can be explored by drilling. For example, drilling during IODP NanTroSEIZE Project (expeditions 314, 315 and 316 and ensuing expeditions) crossed the shallow part of the SW Japan Nankai accretionary prism main megasplay fault and succeeded in obtaining fluid and rock samples (Kimura et al., 2007; Kimura et al., 2008; Strasser et al., 2009; Kinoshita et al., 2009; Sakaguchi et al., 2011; Yamaguchi et al., 2011). However, the deeper parts of megasplay faults, which are the targets of future IODP drilling, are less easy to reach and coring of long sections will probably be challenging.

* Corresponding author. Address: Laboratoire de Géologie, École Normale Supérieure, 24 rue Lhomond, Paris 75005, France. Tel.: +33 144322274.
E-mail address: passelegue@geologie.ens.fr (F.X. Passelègue).

1367-9120/$ - see front matter © 2013 Elsevier Ltd. All rights reserved.
http://dx.doi.org/10.1016/j.jseaes.2013.10.024

Onshore out-of-sequence thrusts (OSTs) exposed in emerged accretionary prisms are regarded as ancient equivalents of offshore active megasplay faults. As such, they have received much attention (Ohmori et al., 1997; Kimura, 1998; Ikesawa et al., 2003; Kondo et al., 2005; Mukoyoshi et al., 2006, 2009; Hara and Kimura, 2008; Rowe et al., 2009). Typically, these OSTs are characterized by lateral extensions of several tens of kilometers, total displacements estimated between 1 and about 10 km, damage zone thicknesses of the order of several tens or hundreds of meters. Moreover, the studied OSTs are thought to have been active at large depths (estimated between 1 km and 10 km) and for significant periods (a few million years). The study of such OSTs can provide complementary information to the offshore equivalents and guidance for future drilling and sampling strategies.

In addition to regional-scale 'first-order' OSTs, other OSTs have also been reported from the Shimanto accretionary prism (Kimura, 1998). These 'second-order' OSTs are truncated by their first-order equivalents, and their surface extensions, offsets and damage thicknesses are less important than those characterizing the first-order OSTs. Despite their lesser importance, the second-order OSTs deserve to be studied. They probably play a role in the hydrological behavior of the whole prism by connecting first-order OSTs between them or by allowing fluid expulsion from the deep parts of the prism (Moore, 1989; Moore and Vrolijk, 1992).

This paper presents the results of a microstructural analysis carried out along a branch of a second-order OST exposed in the Shimanto accretionary prism of SW Japan. Abundant siliceous breccias and fluid paleo-channels in the fault footwall are described and analyzed. A special attention is carried on polyphase breccia cement formation. In particular, fluid inclusions in breccia cements also provide constraints on the pressure and temperature (P–T) conditions of the fluids trapped in the various syn-tectonic cements. The results of these structural and micro-thermometry analyses are integrated in a hydro-mechanical model of the activity of the OST.

2. The Makinokuchi branch of the Nakanomata OST

2.1. Geological setting of the Nakanomata thrust

The Nakanomata out-of-sequence thrust can be followed over about 60 km across Eocene–Oligocene units of the Hyuga Group of the Shimanto Belt in central Kyushu (Fig. 1; Imai et al., 1979, 1982; Kimura et al., 1991; Kimura, 1998; Hara and Kimura, 2008; Hara et al., 2009a,b). It is located between three major, first-order OSTs, the Nobeoka Tectonic Line (NTL) and the Oyabu thrust to the north, and the Ogawa thrust to the south. The geometrical relationships between the Nakanomata OST and the three surrounding first-order OSTs are unknown. On the cross-section of Fig. 2, the Nakanomata OST is considered as truncated by the Ogawa thrust. Total displacement along the Nakanomata OST is about 5 km (Kimura et al., 1991; Kimura, 1998), but significantly decreases in the study area where it is less than 1 km (Hara et al., 2009a).

In the study area, the Nakanomata OST consists of several branches (Hara et al., 2009a). One of these branches, the Makinokuchi branch, is exposed in the bed of the Hitotsuse river, at the Makinokuchi locality (Fig. 2). For a distance of about 50 m, a complete section across the fault can be examined and sampled.

2.2. The Makinokuchi fault zone

The Makinokuchi branch of the Nakanomata OST consists of a planar to slightly undulating, polished and locally striated fault surface separating folded sandstone/siltstone alternations in the hanging-wall from massive sandstones in the footwall. The fault surface, which can be followed along the entire exposure, is interpreted as the most recent slip surface. It has a mean attitude of N70°E-15°NW. Weakly marked striations trend N165°E to N173°E. Folds in the hanging-wall sandstone and siltstone beds are asymmetric and have axes trending N92°E ± 10° and plunging westward of 45° ± 10°. Fold asymmetry is in agreement with a reverse (top-to-the-south) motion along the fault. A 0.5–2 cm thick, indurated, siliceous layer is preserved beneath the fault surface. As detailed below, this layer consists of a siliceous ultracataclasite which is regarded as the most deformed zone (core zone) of the Makinokuchi fault. The footwall consists of a massive sandstone which, with increasing fracturing and brecciation, progressively evolves from a weakly fractured sandstone at a distance of about 4–5 m from the fault to a strongly brecciated and silicified sandstone immediately beneath the ultracataclasite layer (Fig. 3a and b). The hanging-wall sandstone/siltstone beds are only moderately fractured and silicified, with the exception of more important fractured and brecciated sandstones close to the fault, over a thickness of about 50 cm (Fig. 3a and b). The contrast in intensity and thickness of brecciation and silicification between the hanging-wall and the footwall is a key feature of the studied exposure and will be described in the following.

3. Detailed structure of the Makinokuchi fault zone

3.1. Protoliths

3.1.1. Footwall protolith

The footwall protolith is a coarse-grained massive and fractured sandstone. The sandstone is a quartz greywacke (Hara et al., 2009b) consisting of monocrystalline or polycrystalline quartz grains, alkali and plagioclase feldspars, lithic fragments, illite (coating some grains), and minor opaque minerals. The alkaline feldspars are altered and invaded by sericite. The average size of individual grains ranges from 200 to 800 μm. The porosity of the sandstone was not measured. However, porosities between 6% and 12% were obtained in similar coarse-grained sandstones sampled in the footwall of the Nakanomata thrust about 5 km east of the Makinokuchi exposure (Boutareaud, 2007). Thin section counting suggests that the porosity of the intact sandstone at Makinokuchi is about 10%. Diffusive mass transfer (DMT) processes are indicated by stylolitic surfaces and dissolution at grain contacts. The contact between the intact or fractured protolith and the damage zone breccias is progressive and cannot be accurately located.

3.1.2. Hanging-wall protolith

The hanging-wall consists of alternating beds of sandstone and siltstone. The sandstone is a quartz greywacke, but is finer than the footwall sandstone. The average size of individual grains ranges from 30 to 300 μm. The siltstone consists of grains of quartz, plagioclase feldspars, opaque minerals and dominantly phyllosilicates. The average size of individual grains is less than 30 μm. Like in the footwall sandstone, stylolithes and dissolution at grain contacts testify to DMT processes. Here also, the porosity of the sandstone or the siltsone were not measured. However, porosities between 1.5% and 4% were obtained in fine-grained sandstones sampled in the hanging-wall of the Nakanomata thrust about 5 km east of the Makinokuchi exposure (Boutareaud, 2007). Thin section counting suggests that the porosity of the intact hanging-wall sandstone is less porous than the footwall one due to the large amount of clay and the small size of the grains.

3.2. Footwall breccias

Footwall breccias can be divided into three types which are, with decreasing distance to the fault plane, A-, B- and C-type breccias.

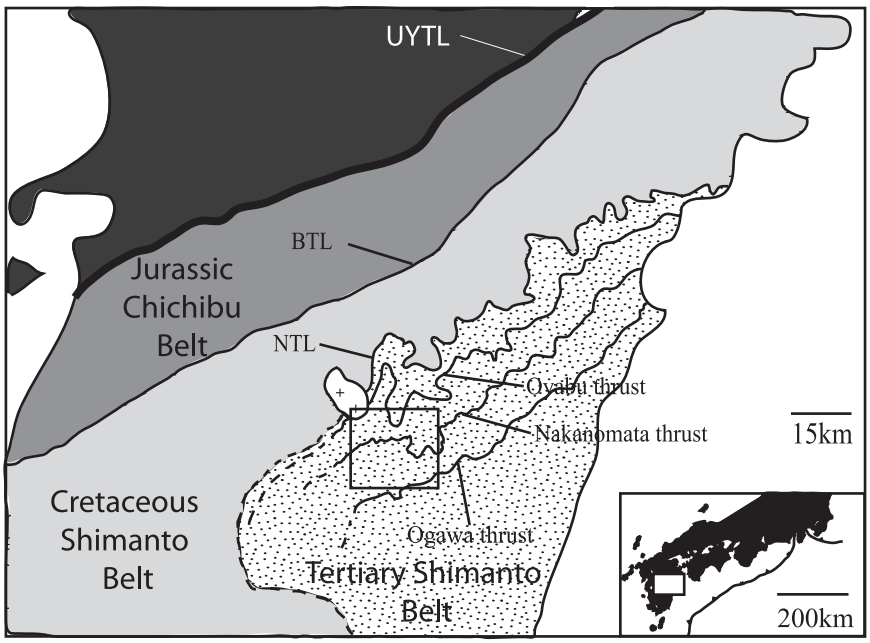

Fig. 1. Geological setting of the study area. UYTL: Usuki-Yatsushiro Tectonic Line. BTL: Butsuzo Tectonic Line. NTL: Nobeoka Tectonic Line.

3.2.1. A-type clast-supported breccias

The clast-supported breccias are the less deformed fault rocks observed in the Makinokuchi fault footwall damage zone. They are observed at a distance of 2–3 m from the fault surface (Figs. 3, 4a and 4b). At the macroscale (outcrop or hand-sample scale), type-A breccias consist of quartz-cemented crackle breccias (Woodcock et al., 2006; Mort and Woodcock, 2008) and show a typical jigsaw puzzle geometry. The clasts, whose sizes are comprised between 5 and 15 cm, are composed of the same sandstone as the one constituting the underlying protolith. They display angular to sub-angular shapes (Fig. 4b). No apparent mutual rotation of the clasts can be detected, suggesting a very weak bulk shear. The fracture traces are irregular and propagate along quartz or feldspar grain junctions (Fig. 5a). The thickness of the cement zone separating two neighbour clasts is comprised between 1 and 10 mm (Figs. 4b and 5a). The average cement-to-clast ratio is 15:85. Optical microscope and cathodo-luminescence observations indicate that the quartz cementing A-type breccias is blocky (Passchier and Trouw, 2005), includes a few tiny clasts and corresponds to a unique episode of cementation. Quartz consists of subhedral crystals with rare euhedral crystals (Fig. 5a), and there is neither open space nor secondary minerals between adjacent crystals. The average size of individual crystals is 300 μm. Stylolithes observed in sandstone clasts do not propagate through the cement, indicating that DMT processes occurred before the brecciation and suggesting that the sandstone was consolidated before faulting. No reworked quartz cement can be found among A-type breccia clasts.

3.2.2. B-type cement-supported breccias

The transition between A-type and B-type breccias is achieved by a progressive increase in the cement-to-clast ratio. B-type breccia has a cement-to-clast ratio of about 40:60 (33:67 to 46:54), and corresponds to a chaotic breccia in the classification of Woodcock et al. (2006) and Mort and Woodcock (2008). The clasts are sub-angular and range in size from 0.4 to 50 mm (Fig. 4c). They predominantly consist of intact sandstone derived from the underlying protolith, but some clasts consist of brecciated sandstone. Such a reworking indicates a polyphase brecciation. The misalignment of the bedding trace preserved in neighbouring clasts and the impossibility of reconstituting the original assemblage indicate that the clasts suffered from mutual rotations (Figs. 4c and 5b). Under the optical microscope, most of the cement (95% in surface abundance) of the B-type breccias is blocky, like that of the A-type breccias. The quartz crystals are subhedral and more rarely euhedral (Fig. 5b). The average size of individual crystals is about 250 μm. There is neither open space nor secondary mineral filling between crystals. Cathodo-luminescence indicates that the B-type breccia cement is homogeneous and corresponds to a unique stage of cementation. Fractures propagated along illite flakes or along grain boundaries, like for A-type breccias. A small percentage (about 5%) of the B-type breccia cement is very fine (average crystal size <100 μm) and contains abundant rock or mineral fragments (microclasts) whose maximum size is less than 200 μm. This cement will be referred to as fine-grained cement. In B-type breccias, the fine-grained cement cross-cuts the blocky cement, indicating that the formation of the fine-grained cement is posterior to that of the blocky cement.

3.2.3. C-type cement-supported breccias

The C-type breccia shows a cement-to-clast ratio of ~70:30. This breccia, which corresponds to a chaotic breccia in the classification of Mort and Woodcock (2008), is characterized by clasts whose sizes range from 0.1 to 40 mm (Fig. 4d). This clast size distribution is wide, and the smallest clasts may not be easily distinguished from the cement crystals. Unlike the breccia types described above, the C-type breccia includes clasts of varied natures: sandstone clasts predominate, but siltstone or mudstone clasts are also present (Figs. 4d, 5c and d). The misalignment of the bedding traces implies that the clasts underwent significant rotations during or after brecciation (Fig. 5c and d). The cement of C-type breccias is blocky or fine-grained. The blocky cement shows the same characteristics as the one observed in A- or B-type breccias (Fig. 5d). The fine-grained cement is composed of fine (maximum length <100 μm) subhedral to anhedral quartz crystals (Figs. 4c and 5d). It also includes a non-negligible proportion (about 25% in area percentage) of mono-mineralic or poly-mineralic microclasts whose sizes are comprised between 10 and 100 μm. These microclasts are composed of well-rounded (detrital) quartz

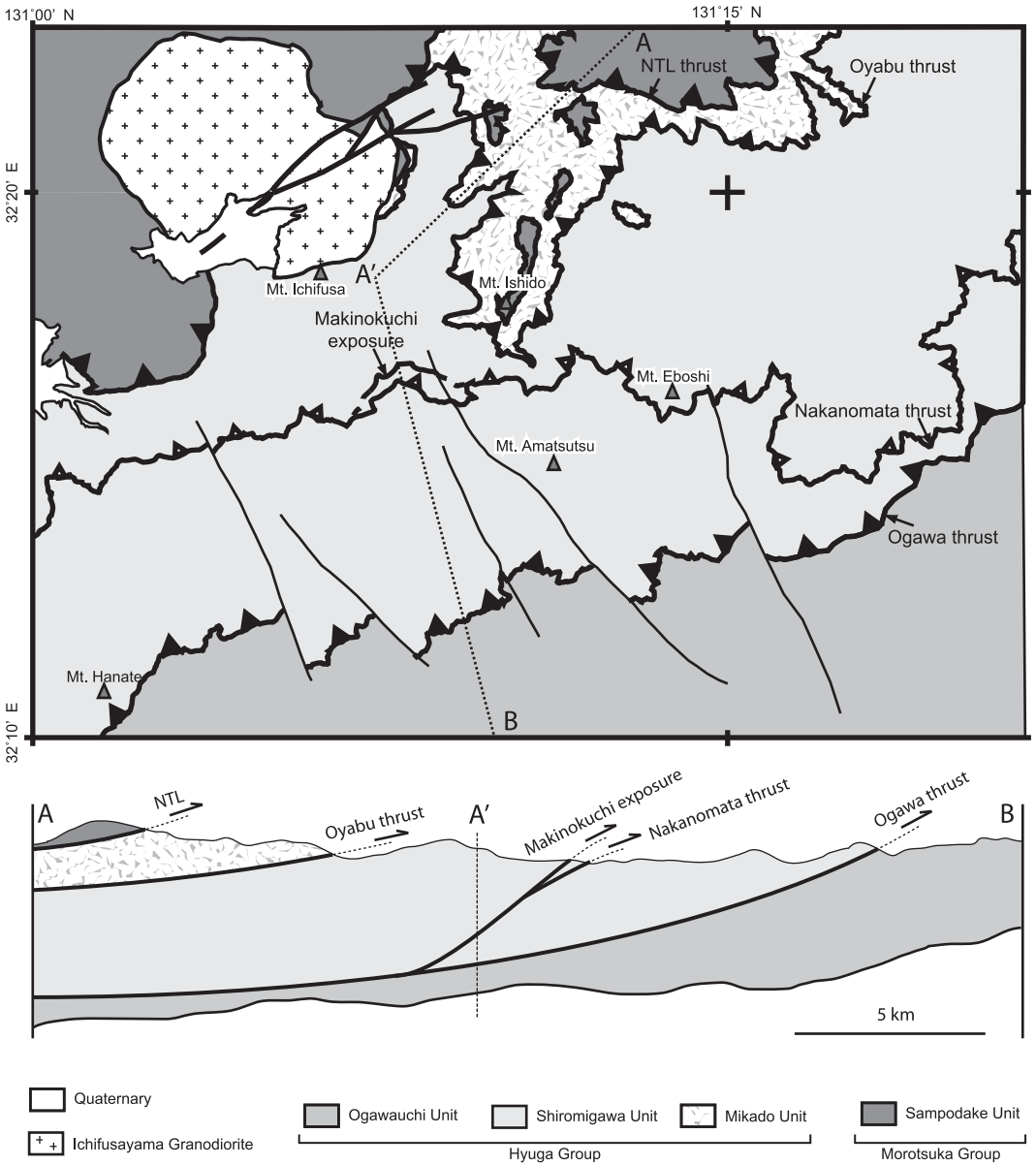

Fig. 2. Structural sketch map of the study area (modified after Kimura et al., 1991, and Hara et al., 2009a) and interpretative cross-section (dashed line A-A'-B on the map). Age of the Sampodake Unit is Late Cretaceous, age of the Huyga Group is Eocene to Oligocene, age of the Ichifusayama granodiorite is Middle Miocene.

grains and needle-shaped (detrital) phyllosilicates. Unlike what is observed in B-type breccias, the chronology between the blocky cement and the fine-grained cement in C-type breccias is not straightforward. The blocky cement can be cross-cut by the fine-grained cement, but the reverse relationship is also observed. This leads to the distinction, in the C-type breccia, of two generations of blocky cements: blocky-1 cement which was formed before the fine-grained cement, and blocky-2 cement which was formed after the fine-grained cement. This chronology is confirmed by the observation, in some C-type breccia thin sections, of clasts constituted by clast-cement assemblages derived from previously formed breccias. These observations suggest that C-type breccias result from several stages of brecciation and cementation.

3.3. Ultracataclasite

A 0.5–2 cm thick, indurated, siliceous ultracataclasite zone is preserved everywhere beneath the fault surface. It clearly truncates the underlying C-type breccia. Under the optical microscope, the ultracataclasite is composed by fine grains which range in size from 15 to 40 μm. Larger grains with sizes about 100–150 μm are scattered inside finer grains. Among these larger grains, breccia or cement fragments can be recognized. The ultracataclasite zone is crossed by quartz veins making angles of 45–50° with the upper fault surface. These veins are interpreted as tension (T-type) fractures (Fig. 6). Their arrangement is in agreement with the reverse sense of shear inferred for the displacement along the upper fault surface.

3.4. Feeder veins

Several steeply-dipping brecciated and silicified feeder veins cross-cut the intact or brecciated footwall and merge with the footwall breccias (Fig. 3). One of these veins (Fig. 3c) is bounded by a sub-vertical plane on one side and by a 70°-dipping plane on the other side. None of the planes is striated. The thickness of the vein

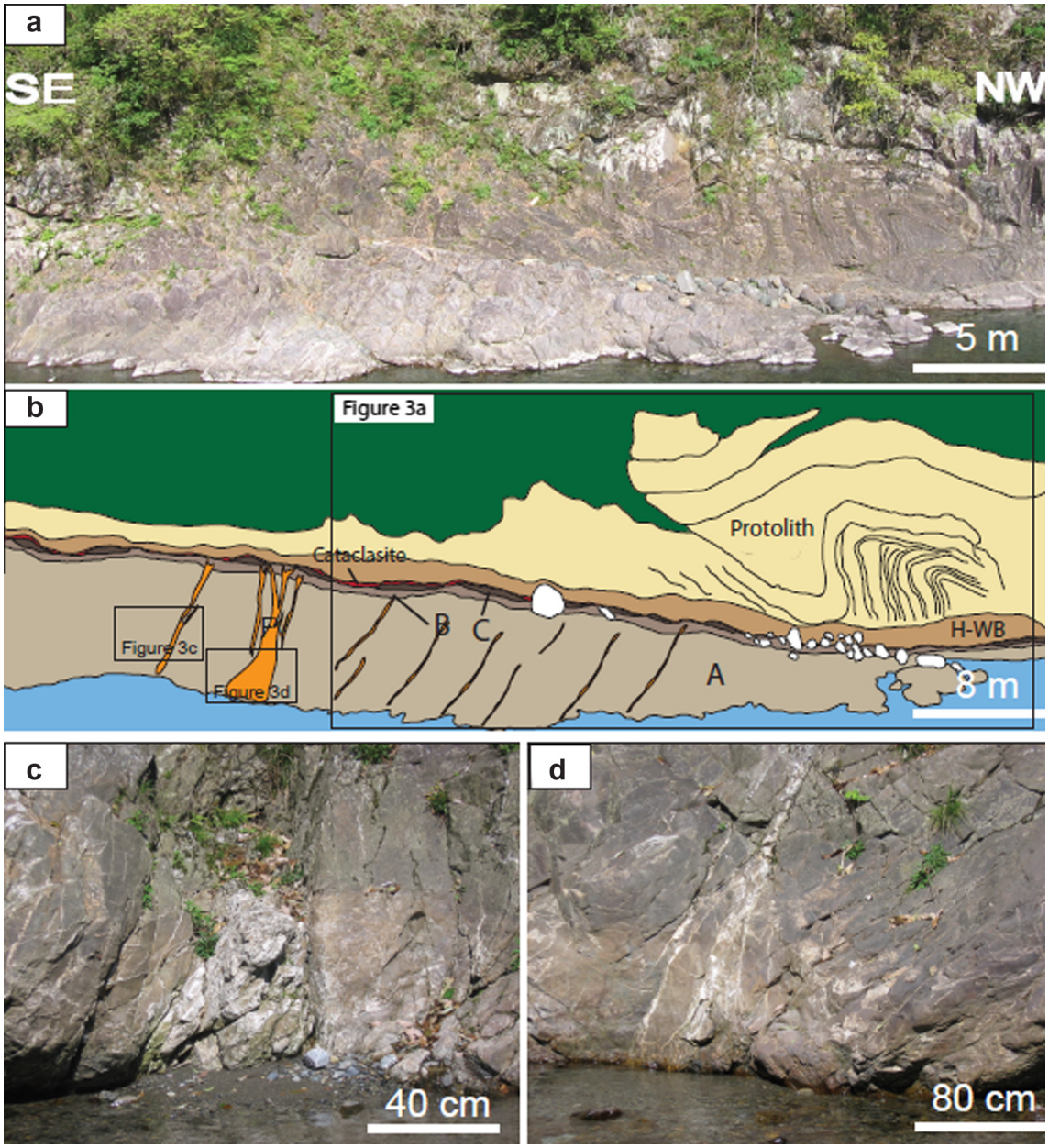

Fig. 3. Exposure of the Makinokuchi branch of the Nakanomata OST. (a) General view. (b) Structural sketch of (a). A: A-type breccias; B: B-type breccias; C: C-type breccias; H-WB: hanging-wall breccia; FV: feeder veins. (c) and (d): close view on the footwall feeder veins.

decreases from 80 cm at its exposed lower part to 45 cm at its upper part, before merging with the breccia. The feeder vein itself consists of quartz veins anastomosed around sandstone fragments. The sandstone fragment/quartz vein ratio is about 70% (surface abundance estimate). The thickness of most quartz veins is comprised between 2 mm and 5 cm, but some veins can be as thick as 10 cm. The second exposed feeder vein is bounded by two 60°-dipping unstriated planes, is 10–15 cm thick, and consists almost entirely of quartz (Fig. 3d). Due to weathering and patina, the upper boundaries of the two feeder veins are unclear. The progressive transition with the overlying breccia and the high quartz content suggest that the two feeder veins are ancient supply conduits of silica-rich fluids. Microscopically, the feeder veins consist of subhedral to euhedral quartz crystals whose size depends on the vein width. In the largest veins, the crystal size ranges from 300 to 400 μm. Crystals are elongated perpendicularly to the vein walls and present a syntaxial texture with euhedral shapes toward the center of the vein, suggesting a purely extensional opening.

3.5. Hanging-wall breccias

Immediately above the fault surface, the hanging-wall sandstone is intensely brecciated over a thickness of about 40 cm and progressively changes to a moderately brecciated sandstone above. A a distance of 1 m from the fault surface, the sandstone and siltstone layers are no longer brecciated. The intensely brecciated sandstone is a crackle breccia (Woodcock et al., 2006). The clasts have sizes between 2 and 15 cm, are of the same nature as the overlying sandstones and siltstones, and have angular to sub-angular shapes. As for the footwall A-type breccias, there is no apparent mutual rotation of the clasts, suggesting a very weak bulk shear. The thickness of the cement zones between fragments is comprised between 1 and 10 mm. The average cement-to-clast ratio is ~10:90 and rarely up to ~20:80. Optical microscopic observations show the quartz cement is homogeneous and is constituted of subhedral crystals. The size of individual crystals range from 150 to 350 μm. As for footwall breccias (A-type and B-type), the

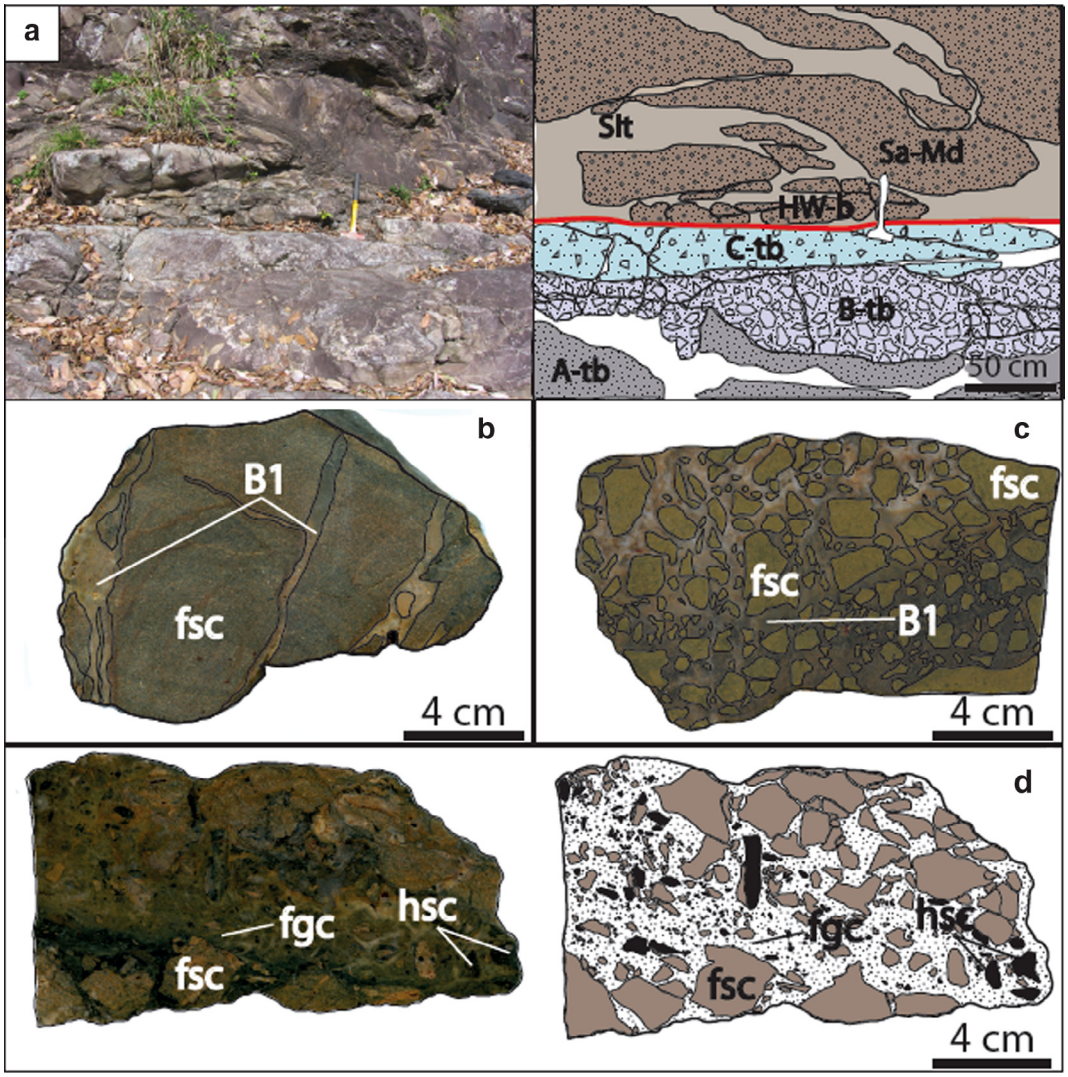

Fig. 4. (a) Close view on the Makinokuchi exposure fault plane and surrounding breccias and corresponding sketch. Abbreviations: A-tb: A-type breccia; B-tb: B-type breccia; C-tb: C-type breccia; HW-b: hanging-wall breccia; Sa-Md: sandstone and mudstone; Slt: siltstone. (b-d) Hand-samples of respectively A-type, B-type and C-type breccias with corresponding sketches. B1: Blocky-1 cement; fsc: footwall sandstone clasts; hsc: hanging-wall sandstone clasts.

fracture traces are irregular and tend to follow grain junctions. In the median part of the cement zones, fine-grained cement can be observed. This late cement shows the same characteristics as the fine-grained cement of the footwall B-or C-type breccias.

3.6. Late-stage veins

Late-stage planar quartz veins cross-cut the footwall of the Makinokuchi fault, whatever brecciated or not (Fig. 3b). They can be followed along distances up to two meters, have thicknesses of up to 5 cm, and consist of quartz without any rock fragments. They clearly cross-cut the footwall breccias. Some of them also cross-cut the ultracataclasite layer, without apparently extending in the hanging-wall. They are therefore younger than the formation of the ultracataclasite but their formation is possibly followed by at least one stage of displacement along the fault surface. Under the microscope, quartz veins consists of granular, subhedral or euhedral crystals that grew perpendicularly to the vein-wall rock boundary, suggesting a purely extensional opening. The instances showing quartz fibres arranged obliquely to the vein boundary remain rare. In the cases where the veins are not completely sealed in their median part, the quartz crystals show euhedral shapes in the center of the veins, whereas they are commonly granular or subhedral near the walls, suggesting a syntaxial growth.

3.7. Summary

The Makinokuchi fault exposure is characterized by quartz-cemented breccias and minor ultracataclasite (Fig. 6). Breccias are more developped in the footwall side than in the hanging-wall side (Fig. 6). In the footwall side, there is a progressive transition from A-type breccia to B-type and to C-type breccias. Only proto-breccia is preserved on the hanging-wall side. Another difference between the two sides of the fault is the presence, in the footwall, of feeder veins which progressively merge with breccias. Microscopically, breccia cements show two morphologies: a blocky morphology observed in all types of breccias on either side of the fault surface (Figs. 4 and 5), and a fine-grained morphology found in B- and C-type footwall breccias and hanging-wall breccias (Fig. 5c and d). In C-type breccias, thin section scale cross-cutting relationships allow to distinguish two generations of blocky cements, one (called blocky-1 cement) being older than the fine-grained one, the other (called blocky-2 cement) being younger. This succession of three

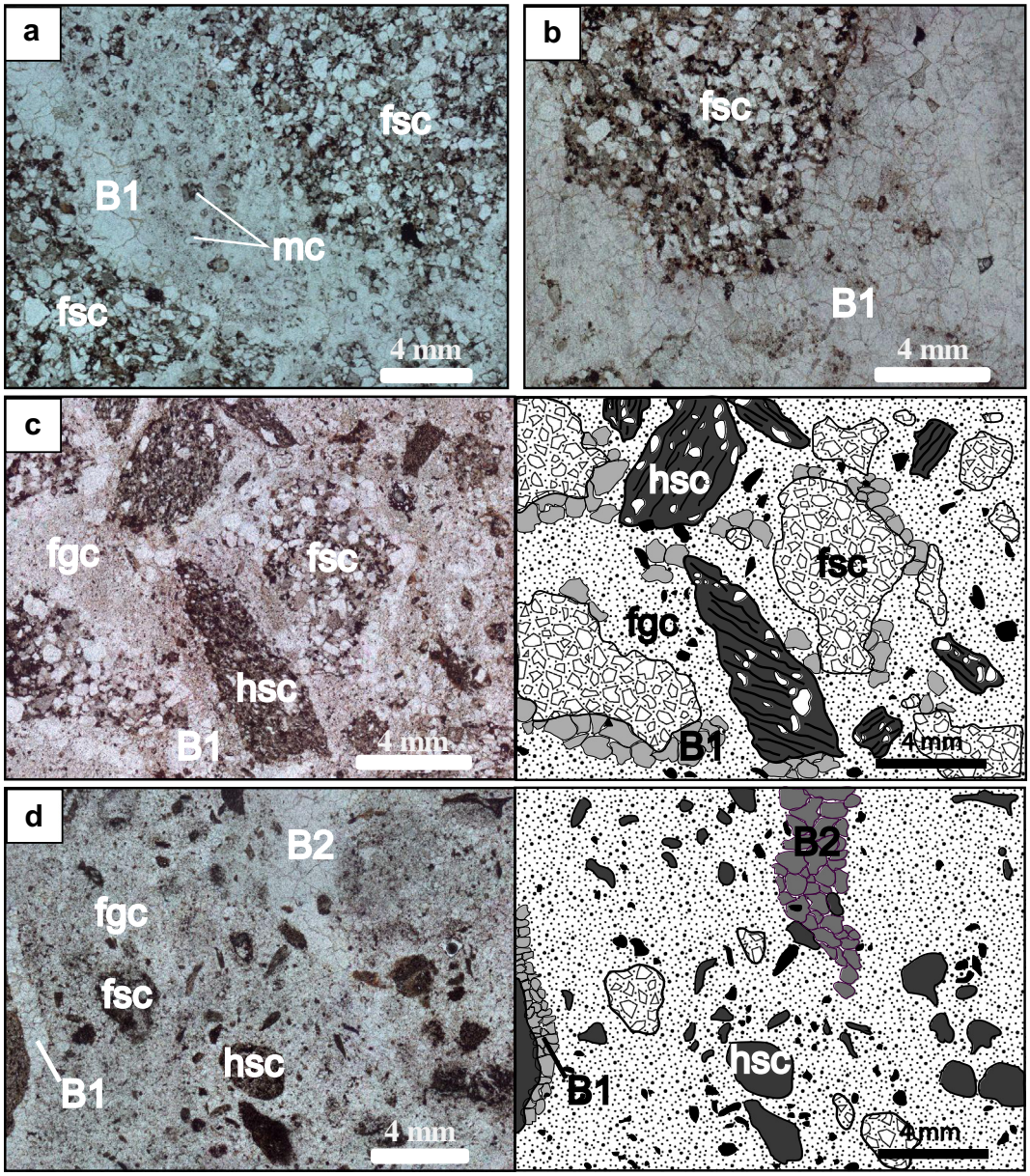

Fig. 5. Photomicrographs of footwall breccias illustrating the different cement types and their cross-cutting relationships. Abbreviations: fsc: footwall sandstone clasts; hsc: hanging-wall sandstone/siltstone clasts, mc: microclasts, B1: blocky-1 cement, B2: blocky-2 cement, fgc: fine-grained cement. (a) A-type breccia with footwall-derived sandstone clasts (fsc) embedded in the blocky-1 cement (bc). Microclasts (mc) are also included in the cement. (b) Cement type 1 in B-type breccia. The degree of silicification is higher than in A-type breccia but the cement presents the same texture. (c) Photomicrograph of C-type breccia. Misalignement of bedding trace in hanging-wall clasts implies significant rotation. Fine grained cement cross-cuts blocky-1 cement. (d) Photomicrographs of C-type breccia. Cross-cutting relationships between the fine-grained cement and blocky cements: Blocky-1 cement is cross-cut by fine-grained cement, blocky-2 cement cross-cuts fine grained cement.

stages of cement formation (blocky-1 cement/fine-grained cement/blocky-2 cement) suggests a cyclic fluid flow.

4. Fluid inclusion analyses

4.1. Methods

Micro-thermometric analyses were done on fluid inclusions trapped in quartz from cements of A-type, B-type and C-type breccias, from fluid conduits and from hanging-wall breccias (Table 1). The analyses were performed by using the standard methods of Roedder (1984) and Shepherd et al. (1985). Fluid inclusions were analyzed on doubly polished thin sections. Sections were about 50 μm thick and glued on glass plates by Geoptic resin. Micro-thermometric measurements and Raman micro-spectrometry were done at the University Lille 1 with a USGS-type (FLUID INC) heating and freezing stage. Calibration of the micro-thermometric stage was made with synthetic fluid inclusions (SYNFLINC; Sterner and Bodnar, 1984) including pure water (ice melting temperature 0.0 °C; critical homogenization temperature 374.1 °C), H_2O–CO_2 inclusions (CO_2 melting temperature −56.6 °C; hydrate melting temperature 10.0 °C) and H_2O–NaCl inclusions (eutectic temperature −21.2 °C). Accuracy is ±0.1 °C for temperatures between −56.6 °C and 25 °C and ±1 °C at 400 °C. All micro-thermometric observations were done carefully in order to avoid any damage to the inclusions. Partial decrepitation of inclusions occurred in rare instances during examination at high temperatures. Raman microspectrometry was done with the techniques of Pasteris and Chou (1998). Raman spectra were recorded

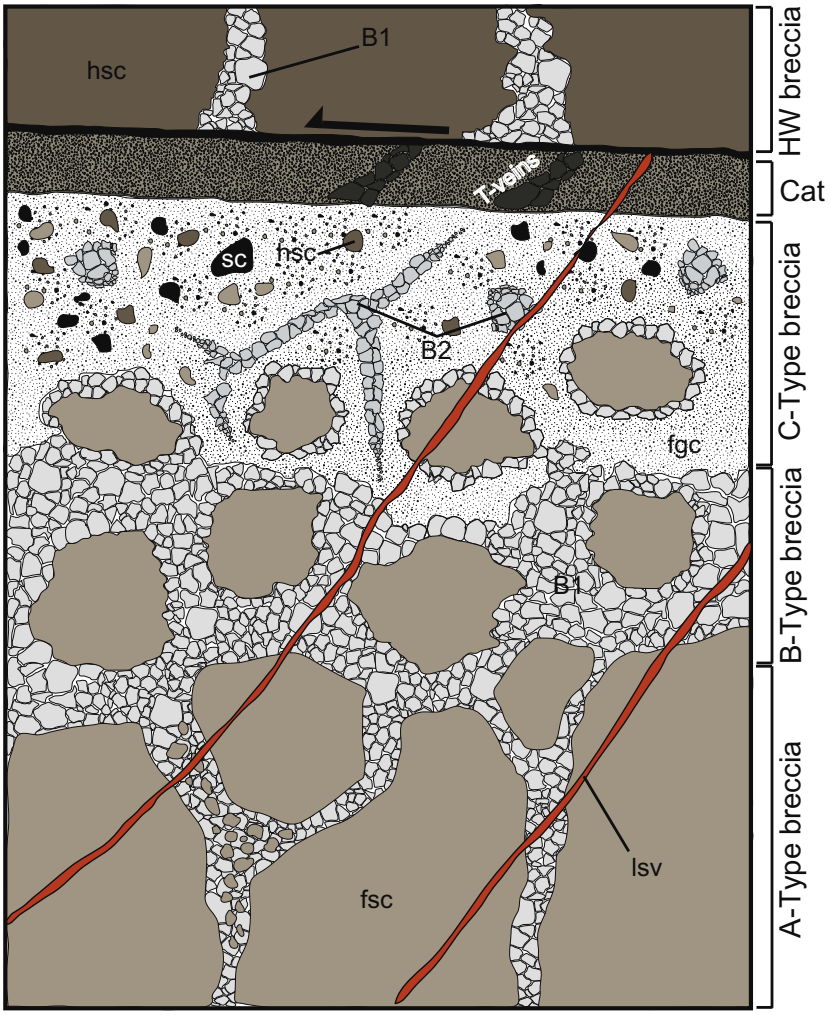

Fig. 6. Sketch summarizing the different cement generations on either side of the Makinokuchi branch fault surface. Abbreviations: fsc: footwall sandstone clasts; hsc: hanging-wall sandstone/siltstone clasts, mc: microclasts, B1: blocky-1 cement, B2: blocky-2 cement, fgc: fine-grained cement, lsv: late stage veins.

Table 1
Vapor-rich fluid inclusions data.

Samples	N freezing	N heating	CH_4 pressure (Bars)	T_H (°C)	T_F (°C)	Salinity (% NaCl eq)	Temperature (°C)	Depth
FEC	46	69	5	274	−0.8	1.3	274	5.0–8.2
Type 1 cement	46	51	3	257	−0.6	1.1	266	5.0–8.2
Type 3 cement	32	32	3	269	−0.7	1.2	269	5.0–8.2
HGW	53	53	3	270	−1.0	1.7	270	5.0–8.2

with a LabRam HR800 Jobin–Yvon™ micro-spectrometer equipped with 1800 lines/mm gratings and by using a 532.28 nm (green) laser excitation. Acquisition time span varied from 20 to 60 s during three accumulating cycles. Inclusions were studied following the concept of Fluid Inclusion Assemblage (FIA, Goldstein and Reynolds, 1994; Goldstein, 2003). Each FIA is composed of a few inclusions (generally about 10, but some can include only a few ones) supposed to be representative of the same trapping event.

4.2. Characteristics of fluid inclusions

Studied fluid inclusions come from footwall type-C breccia (4 thin sections), footwall type-B breccia (2 thin sections), footwall fluid feeder veins (3 thin sections) and hanging-wall breccia cement (2 thin sections). Micro-thermometric measurements could not be done on fine-grained cement or on cataclasite, because of the small size of crystals (65 μm maximum average length). Microscopic observation reveals that all studied cements (hanging-wall breccias, footwall breccias, feeder veins) contain the same three types of fluid inclusions: vapor-rich, carbonic and water-rich. All three types were found in all studied thin sections. Based on Roedder (1984) and Goldstein (2003), vapor-rich and carbonic inclusions can be classified as primary, and water-rich inclusions as secondary. Primary inclusions correspond to fluid entrapped during mineral crystallization and are localized inside the host (quartz) mineral. Secondary inclusions are located along intra-crystalline fractures and correspond to the entrapment of the mineralizing fluid that sealed the intra-crystalline fractures. The vapor-rich fluid inclusions are the most abundant type of primary inclusions. Generally, these inclusions range from 5 to 20 μm in size (Fig. 7). The degree of fill (volume of liquid/volume of liquid + vapor) in these inclusions is high, of the order of 0.50–0.75.

4.3. Micro-thermometric and Raman spectrometry results

4.3.1. Vapor-rich inclusions

The vapor-rich inclusions are H_2O–CO_2–CH_4 fluid inclusions. Results of the micro-thermometric and Raman spectrometry analyses are summarized in Table 1, Figs. 7 and 8. Raman analyses on vapor-rich inclusions show narrow peaks between 2915.182 and 2918.687 cm^{-1}, indicating the presence of methane. In addition, the presence of carbon dioxide is indicated by a characteristic Fermi doublet revealed by peaks at 1290 cm^{-1} and 1390 cm^{-1} (Fig. 7). The scarcity of clathrate (detected during the freezing path on seven inclusions on a total of more than 100 analyzed inclusions) indicates a low CH_4 internal pressure. This low internal pressure is confirmed by the position of the Raman peaks at room temperature (Fabre and Couty, 1986). The melting temperature of clathrates is comprised between 12.7 and 15 °C, suggesting an important heterogeneity of the fluid phase.

All vapor-rich inclusions share similar micro-thermometric characteristics. The final melting of ice occurs in the temperature range of −1 to −0.2 °C (Fig. 8a), corresponding to an equivalent NaCl concentration of approximately 0.35–2.35 wt% (Bodnar, 1993). The vapor-rich inclusions from the hanging-wall cement samples show a larger salinity than for the footwall sample inclusions. However, the average salinity indicates a lower value than seawater. Homogenization into a single liquid phase occurs at temperatures between 225 and 300 °C for blocky-1 cement inclusions and between 240 and 310 °C for blocky-2 cement inclusions (Table 1 and Fig. 8b).

4.3.2. Carbonic inclusions

Carbonic inclusions are the second type of primary inclusions. The inclusions range from 5 to 10 μm in size. They typically contain only one visible phase characterized by a high refractive index. This phase is likely gaseous (Roedder, 1984). The presence of up to 10 vol% liquid water phase is undetected because the high relief of the inclusions precludes the identification of a meniscus. Raman analyses performed on carbonic inclusions indicate the presence of CO_2 and CH_4 (Fig. 7) with peaks between 2914.201 and 2914.901 cm^{-1}. Few micro-thermometric measurements were performed on these inclusions because of their small sizes. However, fifteen inclusions could be studied in the footwall (A and C-type breccias and feeders) and hanging-wall breccia cements. Cooling resulted in the formation of CO_2 solids that melted, with subsequent warming, at temperatures of −65 ± 3 °C. These temperatures are lower than the triple point temperature for pure CO_2 (Burruss, 1981), confirming the presence of methane. Homogenization into a single liquid phase is observed around 19 °C, suggesting a high density of methane in carbonic inclusions.

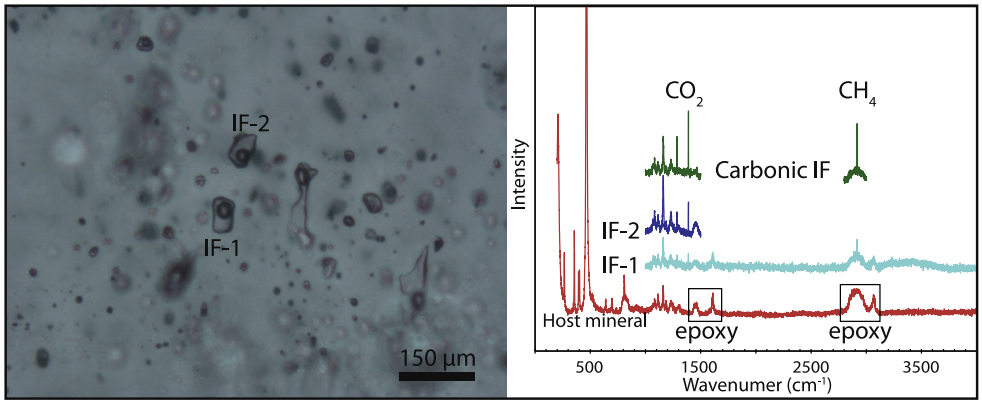

Fig. 7. Photomicrograph of vapor-rich fluid inclusions (IF-1 and IF-2) and corresponding laser Raman spectra in blocky-2 cement.

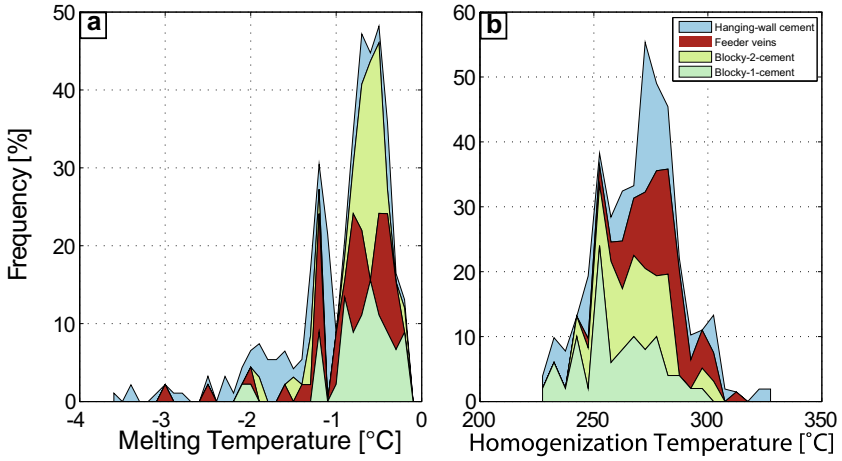

Fig. 8. Ice melting temperatures and homogenization temperatures obtained from vapor-rich fluid inclusions.

5. Interpretation of micro-thermometric results

5.1. Geothermal paleo-gradient

Estimates of the geothermal paleo-gradient in the Shimanto Tertiary sub-belt are not laterally constant. High geothermal gradients (40–110 °C/km) were determined in Tertiary units from the Muroto peninsula in Shikoku (Underwood et al., 1993; Sakaguchi, 1999; Lewis et al., 2000). These high gradients are tentatively explained by the subduction of the Kula-Pacific ridge beneath the SW Japan margin (Shimanto complex) in Oligocene times. A weak thermal alteration of carbonaceous matter in sedimentary rocks of the Eocene–Oligocene Hyuga Group in eastern Kyushu suggests a lower geothermal gradient than at Muroto peninsula (Aihara, 1989; DiTullio and Hada, 1993). More precisely, in the Hyuga group of eastern Kyushu, estimates of the geothermal gradient in the vicinity of the Nobeoka Tectonic Line (NTL) are comprised between 28 and 47 °C/km (Kondo et al., 2005). Based on these pieces of information, a geothermal paleo-gradient between 30 and 50 °C/km is tentatively retained for the study area in Oligocene times.

5.2. Trapping conditions of vapor-rich fluid inclusions

Microscopic observations suggest that vapor-rich and carbonic fluid inclusions were trapped coevally. Indeed, both types of inclusions are primary and are found within the same crystals. The two types of inclusion basically contain the same constituents (CH_4 + CO_2 + H_2O). In vapor-rich inclusions, there are variations in the degree of filling in a given FIA, and the homogenization temperature value ranges as well as the salinity value ranges are large (Table 1 and Fig. 8). Clathrates are observed in the largest vapor-rich inclusions during cooling. These observations suggest that the quartz crystals record the trapping of immiscible fluids composed of an aqueous phase that was saturated with respect to CH_4 and CO_2 (Roedder, 1984; Lewis et al., 2000). In this case, the trapping temperature corresponds to the homogenization temperature of the fluid inclusions (Fig. 8b) and the depth of brecciation can be estimated by using lithostatic or hydrostatic gradient.

5.3. P–T deformation conditions along the Makinokuchi fault as deduced from micro-thermometry of vapor-rich fluid inclusions

5.3.1. Pressure and temperature conditions of formation of footwall breccias

Structural and microstructural analyses show that A- and B-type breccias are mainly cemented by blocky-1 quartz cement. This cement contains vapor-rich fluid inclusions. The P–T conditions of formation of the footwall breccias can be deduced from the P–T conditions of formation of the cements using fluid inclusions analysis. Micro-thermometric measurements show that the mean value of the trapping temperature of the vapor-rich inclusions studied in blocky-1 cement is around 257 °C (Table 1, Figs. 8 and 9). Assuming that the fluid inclusions were trapped under lithostatic gradient conditions with a mean rock density of 2750 kg/m^3 and using the paleo-geothermal gradients mentioned above, estimates of the pressure conditions of cementation are between 135 and 230 MPa (Table 1 and Fig. 9). These conditions correspond to a 5.2–8.6 km depth range below sea floor. The same conditions are deduced for the first stage of cementation observed in the C-type breccias.

The younger generation of blocky cement (blocky-2 cement) observed in C-type breccias also contains vapor rich-inclusions. Assuming the same hypotheses as above, the P–T conditions recorded in the blocky-2 cement indicate an average temperature of 269 °C and an average depth of 5.4–9 km. These results indicate that the first stage of cementation recorded in footwall fault breccias present a slightly lower temperature than the second stage. A progressive elevation of temperature could reflect an episode of burial during fault growth.

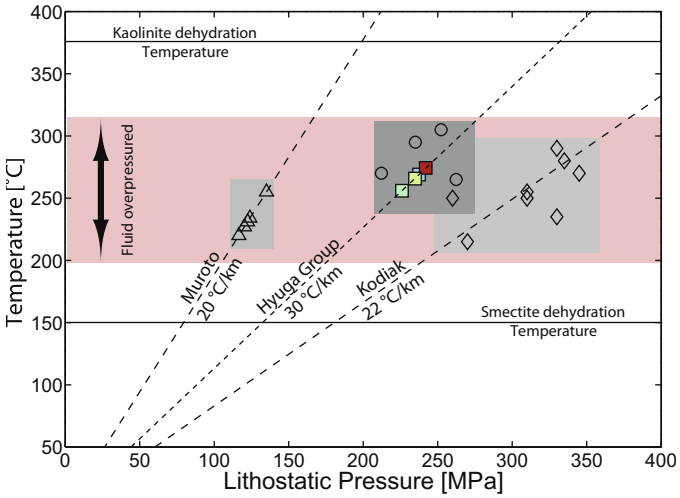

Fig. 9. Summary of average P–T condition obtained from fluid inclusions in quartz veins or cements in Oligocene units. Triangles display data from the Shimanto belt (Muroto area, Ohmori et al., 1997; Sakaguchi, 1999; Lewis et al., 2000; Lewis and Byrne, 2003). Circles display data from the Shimanto belt in the Kyushu area (Kondo et al., 2005). Diamonds display data from Eocene units of the Kodiak accretionary prism (Rowe et al., 2009). Squares represent the results of this study with the same color codes as referred in Fig. 8.

5.3.2. P–T conditions of the formation of feeder and late stage veins

Micro-thermometric data obtained on vapor-rich inclusions from the main quartz cement of the feeder veins and late-stage veins indicate that the temperature of the mineralizing fluids was 274 °C. With the same assumptions as above, estimates of the pressure of the mineralizing fluid correspond to a 5.5–9.1 km depth range below sea floor. The same average conditions are deduced from hanging-wall breccia samples (Fig. 9).

6. Discussion

6.1. Formation of footwall breccias and pore fluid overpressures

The breccias exposed in the footwall of the Makinokuchi fault are clearly dilatant breccias. This is obvious in A-type breccias, which did not undergo any cataclastic flow. These breccias include angular fragments with jigsaw puzzle geometries, suggesting purely extensional openings with effective stresses having overcome the tensile strength of the host sandstone ($pf = \sigma_3 + T_0$, Etheridge, 1983; Price and Cosgrove, 1990; Cosgrove, 1995). The pure extensional opening characteristics is less obvious for B- and C-type breccias, since the clasts remaining in these breccias suffered from pronounced rotation during fluid migration. However, the volumetric predominancy of cement over clast for B- and C-type breccias indicates that they are dilatant breccias. As previously described, at the microscopic scale, the pure extensional characteristic of the footwall breccias is evidenced by the fact that fractures propagated along quartz or feldspar grain junctions without crossing the grains. The lack of zoning in the two types of cements observed in the footwall breccias, particularly the lack of solid inclusion bands or fluid inclusion planes, indicates that opening was not progressive but rather sudden, suggesting pulse-like fluid

overpressures at the fault scale. Even if the cataclasite observed along the main fault surface cannot be easily related to seismic slip, breccias and fragments of host rocks floating in the quartz cements are observed in C-type breccias. These observations can be explained by an extremely high pressure gradient associated with dynamic fracturing during a seismic slip (Sibson, 1988). This hypothesis is supported by the observation of the fine-grained cement near the fault surface, which shows a different texture than that of the blocky type cement. Comparable cement textures are observed along seismogenic faults (Boullier et al., 2004; Caine et al., 2010). This particular texture of fine-grained cement can be attributed by a fluid pressure drop thought to immediately follow co-seismic hydraulic fracturing (Sibson, 1988). In addition, a strong fluid pressure drop could explain the fluid unmixing (Fisher et al., 1995) revealed by the fluid inclusions analyses described above. Alternatively, recent experimental studies revealed that seismic slip in quartz rock induces the formation of a layer of silica gel along the fault plane (Goldsby and Tullis, 2002; Di Toro et al., 2004; Kirkpatrick et al., 2013). The fine-grained cement could be the result of the subsequent recrystallization of a silica gel generated during the seismic slip. However, the large amount of fine-grained cement in C-type breccia, even at 10 cm of the fault plane, suggests that the first hypothesis (fluid pressure drop) remains the best explanation.

6.2. Origin of fluid and P–T conditions of fault activity

The polyphase cementation in C-type breccias, evidenced by the 'blocky cement/fine-grained cement/blocky cement' succession and also by the presence of reworked A-type breccia fragments, reflects a cyclic fluid overpressuring, suggesting a cyclic fault activity. Raman spectrometry of fluid inclusions from footwall breccias, hanging-wall breccia and feeder veins shows that trapped fluids share similar characteristics. They are immiscible and are composed of an aqueous phase saturated with carbonic species. These fluids have the same compositional characteristics than those observed at fluid seepages on the seafloor along traces of active (first-order) OST in accretionary prisms (Carson et al., 2003; Park et al., 2000; Riedel et al., 2002). Similar fluid characteristics are reported from cements of the damage zones of fossil OSTs in the Shimanto Belt (Kondo et al., 2005) and in the Kodiak accretionary prism in Alaska (Rowe et al., 2009). In the present case, Raman analyses of primary vapor-rich inclusions reveal that the aqueous phase presents a salinity lower than the salinity of sea water. This low salinity can be explained by the dehydration of phyllosilicates which induces low-chloride anomalies in active accretionary prism (Henry and Bourlange, 2004; Saffer and McKiernan, 2009). Dehydration is an important sediment consolidation process associated with the seismogenic zone (150–350 °C; Vrolijk, 1990; Hyndman et al., 1997). Mineral dewatering in the subducting oceanic crust and sediments therefore appears as a probable source of fluids. The increase in pore pressure with depth in accretionary prisms, due to the progressive compaction of sediments, generates a pore pressure gradient with the hydrostatic pressure closed to the seafloor (Saffer and Bekins, 2002). This gradient induces the migration of the fluids trapped in the prism along other the seafloor.

Micro-thermometric measurements on fluid inclusions preserved in syn-tectonic cements indicate that the fluids were trapped under the same P–T conditions. These conditions are similar to those of the seismogenic zone of active prisms (Oleskevitch et al., 1999) and to those observed along others fossil out-of-sequence thrusts (Kondo et al., 2005; Rowe et al., 2009) (Fig. 9). Even if the average temperature recorded in the blocky-1 cement is a slightly lower temperature (257 °C), trapping temperatures of fluid inclusions from the blocky-2 cement, from the hanging-wall breccias cement and from the feeder veins cement are similar, respectively 267 °C, 269 °C and 271 °C (average values), suggesting a similar stage of fluid circulation along the fault. These results confirm the role of fluid supply played by the feeder veins during the fault growth. The dilatancy observed in breccias and the relationships between the breccia bodies and the feeder veins suggest that the fluid flow and precipitation occurred during fault activity. The fact that similar P–T conditions of cement formation are recorded on either side of the Makinokuchi fault suggest that the offset was not large enough to offset paleo-isothermal or paleo-isobaric lines and to leave an imprint in the P–T conditions recorded by fluid inclusions.

6.3. The Makinokuchi fault as a hydraulic barrier

The most striking feature of the Makinokuchi fault exposure is the contrast between the intensely brecciated and silicified footwall and the moderately fractured and weakly silicified hanging-wall. Given the subsequent displacements, the two exposed sides of the faults did not evolve in close vicinity, but rather at distance one from the other. Since the exact separation between the two exposed sides of the fault is unknown, this distance cannot be estimated. It is nevertheless likely that fluid overpressures evidenced in the footwall did not significantly propagate through the fault surface into the hanging-wall. A regional survey in the vicinity of the studied fault exposure did not reveal the existence of silicified breccias (comparable to the footwall breccias) in outcrops located in the hanging-wall side of the fault. The Makinokuchi fault likely acted as a barrier with respect to fluids ascending from the footwall and towards the fault surface. The barrier role of the fault can be explained by the fact that the dominant rock types in the hanging-wall are fine-grained sandstones and very fine-grained siltstones. In either case, these rocks are significantly finer and less porous than the footwall coarse-grained sandstone. Though not measured, their permeabilities are likely lower than those in the footwall sandstone.

A similar contrast between a weakly brecciated/silicified hanging-wall and a strongly brecciated/silicified footwall has been reported from other OSTs exposed in the Shimanto accretionary prism (Nobeoka Tectonic Line, Kondo et al., 2005; Mukoyoshi et al., 2009) or in the Kodiak accretionary prism (Uganik thrust, Rowe et al., 2009). Unlike the footwall damage zone of the Makinokuchi branch of the Nakanomata thrust, for which fracturing, brecciation and silicification are mostly developed over 5 m, the thicknesses of the footwall damage zone of both the NTL and the Uganik are of the order of 250 m. This thickness contrast likely reflects differences in the amount of displacements between first-order and second-order OSTs.

The possible barrier role of the Makinokuchi fault can account for the development of fluid overpressures along or below the fault. Following an increase in tectonic compaction, footwall sandstone pore water flew upward through diffuse flow (at large distances from the fault) or through the feeder veins (close to the fault), and accumulated beneath the fault surface, leading to episodic overpressure pulses.

A question which remains unanswered when addressing the past activity of the Makinokuchi fault is to determine whether the motion along the fault pumped the fluids from the footwall sandstones or, to the contrary, whether the fluid pressure build-up (caused for instance by a progressive tectonic compaction of the footwall sandstone) triggered fault motion.

7. Conclusion

Several direct or indirect observations suggest that fluids flow along megasplay faults in active accretionary prisms: fluid seep-

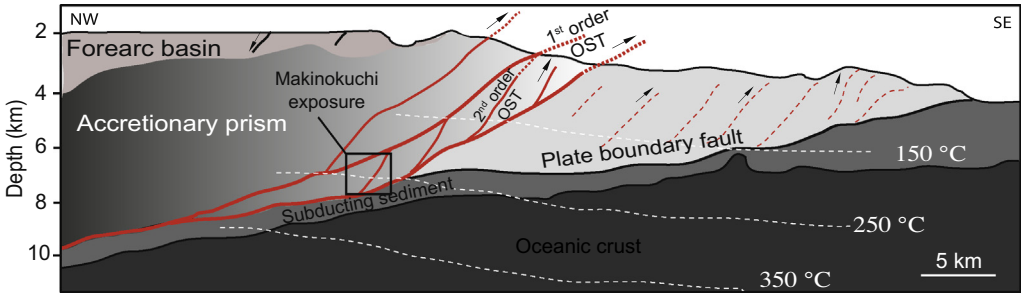

Fig. 10. Possible location of the Nakanomata second-order OST and its Makinokuchi branch within a cross-section of the Shimanto accretionary prism at Oligocene times. Isothermal lines are deduced from the paleo-geothermal gradient (Kondo et al., 2005). The cross-section is drawn after a seismic profile across the present-day Nankai accretionary prism (Moore et al., 2007, 2009).

ages and benthic colonies of invertebrates reported along fault traces at the seafloor, reverse polarities of seismic reflections (Park et al., 2002). As detailed above, evidence for fluid flow and fluid overpressuring along first-order OSTs in emerged accretionary prisms are also abundant (Kondo et al., 2005; Mukoyoshi et al., 2009; Rowe et al., 2009). Besides, recent seismic reflection profiles show that second-order faults merge with first-order megasplay faults or connect two megasplay faults together (Fig. 10). These relationships are clearly visible on the seismic profiles of Moore et al. (2007, 2009) in the Nankai accretionary prism, and can be inferred on the seismic profiles obtained by Collot et al. (2008) across the north Ecuador-south Colombia oceanic margin or from the hypocenter distribution of aftershocks following the 2004 Mw 9.2 Sumatra–Andaman earthquake (Waldhauser et al., 2012). A similar relationship is inferred between the second-order Nakanomata OST (including its Makinokuchi branch) and the structurally above-lying and underlying NTL, Oyabu thrust and Ogawa thrust (Fig. 2). Evidence for fluid flow and for fluid overpressure along the Nakanomata OST Makinokuchi branch suggests that fluid may flow further structurally upward before eventually reaching the above-lying first-order OSTs. Our study suggests that second-order OSTs may play an important role in the hydrogeological organization of accretionary prism with possible implications on the stability of major faults.

Acknowledgments

We thank the associate editor and the reviewer for their constructive remarks which helped to enhance this paper. F. X. P. thanks Henri Leclère and Brice Lacroix for fruitful discussions.

References

Aihara, A., 1989. Paleogeothermal influence on organic metamorphism in the neotectonics of the Japanese Islands. Tectonophysics 159, 291–305.
Bodnar, R.J., 1993. Revised equation and table for determining the freezing point depression of H2O-NaCl solutions. Geochimica et Cosmochimica Acta 57, 683–684.
Boullier, A.-M., Fujimoto, K., Ohtani, T., Roman-Ross, G., Lewin, E., Ito, H., Pezard, P., Ildefonse, B., 2004. Textural evidence for recent co-seismic circulation of fluids in the Nojima fault zone, Awaji island, Japan. Tectonophysics 378, 165–181.
Boutareaud, S., 2007. Slip-weakening mechanism at high slip-velocities: insights from analogue and numerical modeling. PhD Thesis, University of Franche-Comté, pp. 191.
Burruss, R.C., 1981. Analysis of phase equilibria in C–O–H–S fluid inclusions. In: Fluid inclusions: Applications to petrology. Mineralogical Association of Canada, 39–74.
Caine, J.S., Bruhn, R.L., Forster, C.B., 2010. Internal structure, fault rocks, and inferences regarding deformation, fluid flow, and mineralization in the seismogenic Stillwater normal fault, Dixie Valley, Nevada. Journal of Structural Geology 32, 1576e–1589e.
Carson, B., Kastner, M., Bartlett, D., Jaeger, J., Jannasch, H., Weinstein, Y., 2003. Implications of carbon flux from the Cascadia accretionary prism: results from long-term, in situ measurements at ODP Site 892B. Marine Geology 198, 159–180.
Collot, J.Y., Agudelo, W., Ribodetti, A., Marcaillou, B., 2008. Origin of a crustal splay fault and its relation to the seismogenic zone and underplating at the erosional north Ecuador–south Colombia oceanic margin. Journal of Geophysical Research 113, B12102. http://dx.doi.org/10.1029/2008JB005691.
Cosgrove, J.W., 1995. The expression of hydraulic fracturing in rocks and sediments. Geological Society of London Special Publication 92, 187–196.
Cummins, P.R., Kaneda, Y., 2000. Possible splay fault slip during the 1946 Nankai earthquake. Geophysical Research Letters 27, 2725–2728.
Cummins, P.R., Hori, T., Kaneda, Y., 2001. Splay fault and megathrust slip in the Nankai Trough. Earth, Planets and Space 53, 243–248.
Di Toro, G., Goldsby, D.L., Tullis, T.E., 2004. Friction falls towards zero in quartz rock as slip velocity approaches seismic rates. Nature, 427.
DiTullio, L., Hada, S., 1993. Regional and local variations in the thermal history of the Shimanto Belt, Southwest Japan. In: Underwood, M.B. (Ed.), Thermal evolution of the Tertiary Shimanto Belt, southwest Japan: an example of ridge-trench interaction. Geological Society of America Special Paper 273, 103-114.
Etheridge, 1983. Differential stress magnitudes during regional deformation and metamorphism: upper bound imposed by tensile fracturing. Geology 11, 231–234.
Fabre, D., Couty, R., 1986. Etude, par microspectrométrie Raman, du méthane comprimé jusqu'à 3 kbar. APPLICATION à la mesure de pression dans les inclusions fluides contenues dans les minéraux. Comptes-Rendus de l'Académie des Sciences de Paris 303, 1305–1308.
Fisher, D.M., Brantley, S.L., Everett, M., Dzvonik, J., 1995. Cyclic fluid flow through a regionally extensive fracture network within the Kodiak accretionary prism. Journal of Geophysical Research 100, 12881–12894.
Goldsby, D.L., Tullis, T.E., 2002. Low friction strength of quartz rocks at subseismic slip rates. Geophysical Research Letters 29, 1844.
Goldstein, R.H., Reynolds, T.J., 1994. Systematics of fluid inclusions in diagenetic minerals. SEPM short course. Society for, Sedimentary Geology 31, 199 p.
Goldstein, R.H., 2003. Petrographic Analysis of Fluid Inclusions. Mineralogical Association of Canada, Vancouver, Canada, 9–53.
Hara, H., Kimura, K., 2008. Metamorphic and cooling history of the Shimanto accretionary complex, Kyushu, Southwest Japan: implications for the timing of out-of-sequence thrusting. Island Arc 17, 546–559.
Hara, H., Kimura, K., Naito, K., 2009. Geological Map of Japan 1:50000. Murasho, Geological Survey of Japan, AIST.
Hara, H., Kimura, K., Naito, K., 2009b. Geology of the Murasho District. Quadrangle Series, 1:50,000. Geological Survey of Japan, AIST, 56 p. (in Japanese with English abstract 3 p.).
Henry, P., Bourlange, S., 2004. Smectite and fluid budget at Nankai ODP sites derived from cation exchange capacity. Earth and Planetary Science Letters 219, 129–145.
Hsu, S.K., Yeh, Y.C., Sibuet, J.C., Doo, W.B., Tsai, C.H., 2013. A mega-splay fault system and tsunami hazard in the southern Ryukyu subduction zone. Earth and Planetary Science Letters 362, 99–107.
Hyndman, R.D., Yamano, M., Oleskevich, A.D., 1997. The seismogenic zone of subduction thrust faults. Island Arc 6, 244–260. http://dx.doi.org/10.1111/j.1440-1738.1997.tb00175.x.
Ikesawa, E., Sakaguchi, A., Kimura, G., 2003. Pseudotachylyte from an ancient accretionary complex: evidence for melt generation during seismic slip along a master decollement? Geology 31, 637–640.
Ito, Y., Obara, K., 2006a. Dynamic deformation of the accretionary prism excites very low frequency earthquakes. Geophysical Research Letters 33, L02311. http://dx.doi.org/10.1029/2005GL025270.
Ito, Y., Obara, K., 2006b. Very low frequency earthquakes within accretionary prism are very low stress-drop earthquakes. Geophysical Research Letters 33, L09302. http://dx.doi.org/10.1029/2006GL025883.
Imai, I., Teraoka, Y., Okumura, Y., 1979. Geological Map of Japan 1:50000. Mikado, Geological Survey of Japan, AIST.
Imai, I., Teraoka, Y., Okumura, Y., 1982. Geological Map of Japan 1:50000. Morotsukayama, Geological Survey of Japan, AIST.
Kimura, G., Screaton, E.J., Curewitz, D., 2007. Integrated Ocean Drilling Program Expedition 316 Scientific Prospectus NanTroSEIZE Stage 1: NanTroSEIZE Shallow Megasplay and Frontal Thrusts. doi:10.2204/iodp.sp.316.

Kimura, G., Screaton, E.J., Curewitz, D., and the Expedition 316 Scientists, 2008. NanTroSEIZE Stage 1A: NanTroSEIZE shallow megasplay and frontal thrusts. Integrated Ocean Drilling Program Preliminary Report 316, doi: 10.2204/iodp.pr.316.

Kimura, K., Iwaya, T., Mimura, K., Sato, Y., Sato, T., Suzuki, Y., Sakamaki, Y., 1991. Geological Map of Japan 1:50000. Osuzuyama, Geological Survey of Japan, AIST.

Kimura, K., 1998. Out-of-sequence thrust of an accretionary complex. Memoirs of the Geological Society of Japan 50, 131–146.

Kinoshita, M., Tobin, H., Ashi, J., Kimura, G., Lallemant, S., Screaton, E.J., Curewitz, D., Masago, H., Moe, K.T., and the Expedition 314/315/316 Scientists, 2009. Proceedings of the Integrated Ocean Drilling Program, Volume 314/315/316. Washington, D.C., Integrated Ocean Drilling Program Management International Inc., doi: 10.2204/iodp. proc.314315316.133.2009.

Kirkpatrick, J.D., Rowe, C.D., White, J.C., Brodsky, E.E., 2013. Silica gel formation during fault slip: evidence from the rock record. Geology 41 (9), 1015–1018.

Kondo, H., Kimura, G., Masago, H., Ohmori-Ikehara, K., Kitamura, Y., Ikesawa, E., Yamaguchi, A., Okamoto, S., 2005. Deformation and fluid flow of a major out-of-sequence thrust located at seismogenic depth in an accretionary complex: Nobeoka Thrust in the Shimanto Belt, Kyushu, Japan. Tectonics 24. http://dx.doi.org/10.1029/2004TC001655.

Lewis, J.C., Byrne, T.B., Pasteris, J.D., London, D., Morgan, G.B., 2000. Early Tertiary fluid flow and pressure-temperature conditions in the Shimanto accretionary complex of south-west Japan: constraints from fluid inclusions. Journal of Metamorphic Geology 18, 319–333.

Lewis, J.C., Byrne, T.B., 2003. History of metamorphic fluids along outcrop-scale faults in a Paleogene accretionary prism, SW Japan: implications for prism-scale hydrology. Geochemistry, Geophysics, Geosystems 4. http://dx.doi.org/10.1029/2002GC000359.

Melnick, D., Moreno, M., Motag, M., Cisternas, M., Wesson, R.L., 2012. Splay fault slip during the Mw 8.8 2010 Maule Chile earthquake. Geology 40, 251–254. http://dx.doi.org/10.1130/G32712.1.

Moore, J.C., 1989. Tectonics and hydrogeology of accretionary prisms: role of the décollement zone. Journal of Structural Geology 11, 95–106.

Moore, J.C., Diebold, J., Fisher, M.A., Sample, J., Brocher, T., Talwani, M., von Huene, R., Rowe, C., Stevens, C., Sawyer, D., 1991. EDGE deep seismic reflection transect of the eastern Aleutian arc-trench layered lower crust reveals underplating and continental growth. Geology 19, 420–424.

Moore, J.C., Vrolijk, P., 1992. Fluids in accretionary prisms. Reviews of Geophysics 30, 113–135.

Moore, G.F., Bangs, N.L., Taira, A., Kuramoto, S., Pangborn, E., Tobin, H.J., 2007. Three dimensional splay fault geometry and implications for tsunami generation. Science 318, 1128–1131. http://dx.doi.org/10.1126/science.1147195.

Moore, G.F., Park, J.O., Bangs, N.L., Gulick, S.P., Tobin, H.J., Nakamura, Y., Sato, S., Tsuji, T., Yoro, T., Tanaka, H., Uraki, S., Kido, Y., Sanada, S., Kuramoto, S., Taira, A., 2009. Structural and seismic stratigraphic framework of the NanTroSEIZE Stage 1 transect. In: Kinoshita, M., Tobin, H., Ashi, J., Kimura, G., Lallement, S., Screaton, E.J., Curewitz, D., Masago, H., Moe, K.T., and the Expedition 314/315/316 Scientists, Proceedings of the, Integrated Ocean Drilling Program, Volume 314/315/316. doi:10.2204/iodp.proc.314315316.102.2009.

Mort, K., Woodcock, N.H., 2008. Quantifying fault breccia geometry: Dent Fault, NW England. Journal of Structural Geology 30, 701–709.

Mukoyoshi, H., Hirono, H., Hara, H., Sekine, K., Tsushiya, N., Sakaguchi, A., Soh, W., 2009. Style of fluid flow and deformation around an out-of-sequence thrust: An example from the Nobeoka Tectonic Line in the Shimanto accretionary complex, Southwest Japan. Island Arc 18, 333–351.

Mukoyoshi, H., Sakaguchi, A., Otsuki, K., Hirono, H., Soh, W., 2006. Co-seismic frictional melting along an out-of-sequence thrust in the Shimanto accretionary complex. Implications on the tsunamigenic potential of splay faults in modern subduction zones. Earth and Planetary Science Letters 245, 330–343.

Obana, K., Kodaira, S., 2009. Low-frequency tremors associated with reverse faults in a shallow accretionary prism. Earth and Planetary Science Letters 287, 168–174.

Ohmori, K., Taira, A., Tokuyama, H., Sakaguchi, A., Okamura, M., Aihara, A., 1997. Paleothermal structure of the Shimanto accretionary prism, Shikoku, Japan: role of an out-of-sequence thrust. Geology 25, 327–330.

Oleskevich, D.A., Hyndman, R.D., Wang, K., 1999. The updip and downdip limits to great subduction earthquakes: Thermal and structural models of Cascadia, south Alaska, SW Japan, and Chile. Journal of Geophysical Research 104 (14), 965–1014. http://dx.doi.org/10.1029/1999JB900060.

Park, J.O., Tsuru, T., Kodaira, S., Nakanishi, A., Miura, S., Kaneda, Y., Kono, Y., 2000. Out-of-sequence thrust faults developed in the coseismic slip zone of the 1946 Nankai earthquake (Mw = 8.2) off Shikoku, southwest Japan. Geophysical Research Letters 27, 1033–1036.

Park, J.O., Tsuru, T., Kodaira, S., Cummins, P.R., Kaneda, Y., 2002. Splay fault branching along the Nankai subduction zone. Science 297, 1157–1160. http://dx.doi.org/10.1126/science.1074111.

Passchier, C.W., Trouw, R.A.J., 2005. Micro-tectonics. Springer Verlag, pp. 289.

Pasteris, J.D., Chou, I.M., 1998. Fluid-deposited graphite inclusions in quartz: comparison between KTB (German Continental Deep Drilling) core samples and artificially reequilibrated natural inclusions. Geochimica et Cosmochimica Acta 62, 109–122.

Plafker, G., 1972. Alaskan earthquake of 1964 and Chilean earthquake of 1960: implications for arc tectonics. Journal of Geophysical Research 77, 901–925.

Price, N.J., Cosgrove, J.W., 1990. Analysis of Geological Structures. Cambridge University Press, pp. 502.

Riedel, M., Spence, G.D., Chapman, N.R., Hyndman, R.D., 2002. Seismic investigations of a vent field associated with gas hydrates, offshore Vancouver Island. Journal of Geophysical Research 107 (B9), 2200. http://dx.doi.org/10.1029/2001JB000269.

Roedder, E., 1984. Fluid Inclusions. Mineralogical Society of America.

Rowe, C.D., Meneghini, F., Moore, J.C., 2009. Fluid-rich damage zone of an ancient out-of-sequence thrust, Kodiak Islands, Alaska. Tectonics 28. http://dx.doi.org/10.1029/2007TC002126.

Saffer, D.M., Bekins, B.A., 2002. Hydrologic controls on the morphology and mechanics of accretionary wedges. Geology 30, 271–274.

Saffer, D., McKiernan, A.W., 2009. Evaluation of in situ smectite dehydration as a pore water freshening mechanism in the Nankai trough, offshore southwest Japan. Geochemistry Geophysics Geosystems 10, Q02010. http://dx.doi.org/10.1029/2008GC002226.

Sakaguchi, A., 1999. Thermal maturity in the Shimanto accretionary prism, southwest Japan, with the thermal change of the subducting slab: fluid inclusion and vitrinite reflectance study. Earth and Planetary Science Letters 173, 61–74.

Sakaguchi, A., Chester, F., Curewitz, D., Fabbri, O., Goldsby, D., Kimura, G., Li, C.F., Masaki, Y., Screaton, E.J., Tsutsumi, A., Ujiie, K., Yamaguchi, A., 2011. Seismic slip propagation to the up-dip end of plate boundary subduction interface faults: Vitrinite reflectance geothermometry on IODP NanTroSEIZE cores. Geology 39, 395–398. http://dx.doi.org/10.1130/G31642.1.

Shepherd, T.J., Rankin, A.H., Alderton, D.H.M., 1985. A Practical Guide to Fluid Inclusion Studies. Blackie and Son Limited.

Sibson, R.H., Robert, F., Poulsen, K.H., 1988. High angle reverse fault, fluid-pressure cycling and mesothermal gold quartz deposits. Geology 16, 551–555.

Sterner, S.M., Bodnar, R.J., 1984. Synthetic fluid inclusions in natural quartz, I. Compositional types synthesized and applications to experimental geochemistry. Geochimica et Cosmochimica Acta 48, 2659–2668.

Strasser, M., Moore, G.F., Kimura, G., Kitamura, Y., Kopf, A.J., Lallemant, S., Park, J.O., Screaton, E.J., Su, X., Underwood, M.B., Zhao, X., 2009. Origin and evolution of a splay fault in the Nankai accretionary wedge. Nature Geoscience 2, 648–652. http://dx.doi.org/10.1038/NGEO609.

Tanioka, Y., Satake, K., 2001. Detailed coseismic slip distribution of the 1944 Tonankai earthquake estimated from tsunami waveforms. Geophysical Research Letters 28, 1075–1078. http://dx.doi.org/10.1029/2000GL012284.

Underwood, M.B., Laughland, M.M., Kang, S.M., 1993. Acomparison among organic and inorganic indicators of diagenesis and low-temperature metamorphism, Tertiary Shimanto Belt, Shikoku, Japan. In: Underwood, M.B. (Ed.), Thermal evolution of the Tertiary Shimanto Belt, southwest Japan: an example of ridge-trench interaction. Geological Society of America Special Paper 273, 45-61.

Vrolijk, P., 1990. On the mechanical role of smectite in subduction zones. Geology 18, 703–707.

Waldhauser, F., Schaff, D.P., Diehl, T., Engdahl, R., 2012. Splay faults imaged by fluid-driven aftershocks of the 2004 Mw 9.2 Sumatra-Andaman earthquake. Geology 40, 243–246. http://dx.doi.org/10.1130/G32420.1.

Woodcock, N.H., Omma, J.E., Dickson, J.A., 2006. Chaotic breccia along the Dent Fault, NW England: implosion or collapse of a fault void? Journal of the Geological Society, London 163, 431–446.

Yamaguchi, A., Sakaguchi, A., Sakamoto, T., Iijima, K., Kameda, J., Kimura, G., Ujiie, K., Chester, F.M., Fabbri, O., Goldsby, D., Tsutsumi, A., Li, C.F., Curewitz, D., 2011. Progressive illitization in fault gouge caused by seismic slip propagation along a megasplay fault in the Nankai Trough. Geology 39, 995–998. http://dx.doi.org/10.1130/G32038.1.